npj | precision oncology

Article

Published in partnership with The Hormel Institute, University of Minnesota

https://doi.org/10.1038/s41698-026-01465-3

Development of a translational murine model for antibody-drug conjugate-induced interstitial lung disease

Suresh Anaganti[1] ✉, Arti Bhujade[1], Steven Murkli[1], Zachary Sparta[1], Nabin Panth[1], Alexander Weig[1], Richa Vartak[1], Jose Ponte[1], Julien Dugal-Tessier[1] ✉ & Nareshkumar Jain[1,2]

Antibody–drug conjugates (ADCs) have emerged as a promising therapeutic modality, accelerated by the success of topoisomerase I inhibitor-based ADCs. Deruxtecan, the linker–payload in Enhertu®, is transforming HER2+ breast cancer treatment but is linked to severe off-target toxicity, notably interstitial lung disease (ILD), a serious and mechanistically unresolved adverse event. The preclinical prediction of ILD, however, remains poor and largely dependent on non-human primates (NHP). Here, we establish a robust murine model that recapitulates delayed-onset, ILD-like pathology following repeated ADC administration. Mice treated with trastuzumab deruxtecan (T-Dxd) developed progressive pulmonary injury manifested by alveolar septal thickening, inflammatory infiltrates, pneumocyte hyperplasia, and subsequent fibrotic remodeling. These key histopathological changes closely parallel clinical observations and findings reported in non-human primates. Notably, the delayed nature of injury, emerging after repeated dosing rather than acutely, aligns with clinical ILD timing and further underscores the need for extended observation windows in preclinical studies. Using this model, we further demonstrate its ability to differentiate ADCs with distinct pulmonary safety profiles. Under identical dosing paradigms, Trastuzumab and an SN-38-based Trastuzumab-ADC showed minimal lung pathology, supporting the model's ability to distinguish ADCs with divergent pulmonary safety profiles. The model's discriminative capacity was further explored by studying NJB-T-PL119, a novel Trastuzumab-based ADC incorporating an alternative linker–payload. This novel ADC retained antitumor efficacy comparable to T-Dxd yet produced only low-grade pulmonary changes. This platform provides a scalable, ethically feasible, and mechanistically relevant system for early de-risking of ADC-associated lung injury, enabling informed molecule design and prioritization before advancing to NHP toxicology or clinical evaluation.

Antibody–drug conjugates (ADCs) have transitioned from an emerging therapy to an established modality in oncology. By combining the specificity of monoclonal antibodies with the cytotoxic potency of small molecules, ADCs expand treatment options for new patient populations while, in some settings, replacing conventional chemotherapy. This dual-function approach enables selective delivery of highly potent chemotherapeutics to tumors, improving the therapeutic index and limiting systemic exposure[1,2]. Since the first approval of gemtuzumab ozogamicin (Mylotarg®) in 2000 for CD33-positive acute myeloid leukemia, the field has advanced rapidly, with over 14 ADCs approved worldwide and more than 100 in clinical development for both hematologic and solid tumors[3]. As with other modalities, clinical progress has been accompanied by novel toxicities, underscoring the need for improved preclinical models[4].

Among the approved ADCs, Trastuzumab Deruxtecan (T-Dxd) has demonstrated exceptional efficacy in HER2+ breast, gastric, and lung cancers, and is now considered standard of care in several settings[5]. However, its clinical benefit has been constrained by interstitial lung disease (ILD), a serious adverse event. In pooled safety analyses from nine phase I and II trials, the median time to onset of adjudicated ILD events was 5.4 months (range < 0.1–46.8 months), with 87% of cases occurring within the first year

[1]NJ Bio, Inc. (NJ Bio), Princeton, NJ, USA. [2]Aruka Bio, Inc, Princeton, NJ, USA. ✉e-mail: suresh.anaganti@njbio.com; julien.dugal-tessier@njbio.com

The Hormel Institute University of Minnesota

of treatment[6]. Dose-escalation studies in metastatic breast cancer further revealed higher ILD incidence at 6.4 mg/kg (22.7%) compared to 5.4 mg/kg (9.3%), leading to adoption of the lower dose for ongoing development[7]. Real-world post-marketing surveillance has reported similar timelines and severity patterns[8]. In contrast, sacituzumab govitecan (Trodelvy®), which also employs the topoisomerase I inhibitor SN-38, has shown robust efficacy across multiple solid tumors with no clinically significant ILD reported[9,10]. This discrepancy suggests that the key components of ADCs, such as mAbs, payloads, structural features, including linker–payload design, molecular architecture, and biodistribution, may strongly influence pulmonary safety[11].

Non-human primate (NHP) studies lend further support to this concept. T-Dxd induced pulmonary toxicity in cynomolgus monkeys despite low HER2 expression in lung tissue. Repeat dosing at clinically relevant exposures (≥30 mg/kg every three weeks, total 4 doses) produced interstitial pneumonitis characterized by alveolar thickening, lymphocytic infiltration, macrophage accumulation, and fibrosis, consistent with clinical ILD features[12]. Importantly, this NHP model was established retrospectively, as standard GLP toxicology studies did not capture the delayed-onset pulmonary toxicity, which only became apparent with increased and repeated dosing. Notably, administration of unconjugated Dxd monohydrate at higher systemic exposures did not produce similar lesions, implicating that toxicity stems from the full antibody–drug conjugate, not from the payload alone[12]. In contrast, a dedicated nonclinical safety study of the novel anti-CEACAM5 ADC M9140, incorporating a hydrophilic β-glucuronide linker conjugated to the exatecan payload, revealed no pulmonary toxicity in cynomolgus monkeys under protocols directly comparable to those that previously confirmed ILD with T-Dxd[13]. These observations point to meaningful differences in pulmonary response between ADCs and reinforce the need for translational tools capable of identifying ILD-associated liabilities earlier in development. While NHP studies provide critical toxicological insight, they are resource-intensive, lower throughput, and ethically constrained, limiting their practical utility during early discovery and candidate selection phases. To address this gap, we developed a murine model that recapitulates key histopathological hallmarks and timing characteristics of ADC-associated ILD. This platform enables structured and comparative evaluation of ADCs for pulmonary liability prior to NHP testing, supporting earlier and more informed risk assessment in ADC development.

Results

Establishment of a murine model to evaluate ADC-induced interstitial lung disease

To develop a robust murine model of ADC-induced interstitial lung disease (ILD), we selected trastuzumab deruxtecan (T-Dxd), a clinically validated ADC known to cause ILD in patients[14]. Dose selection was guided by previously described non-clinical studies, including those by Kumagai et al.[12]. Based on FDA body-surface-area scaling (km ratio 12/3), a cynomolgus monkey dose of 78.8 mg/kg used in NHP studies translates to approximately 315 mg/kg in mice, underscoring the need for higher murine doses to achieve clinically relevant exposure. However, because ~300 mg/kg dose exceeds murine tolerability limits, a 200 mg/kg dose was selected as a high but feasible exposure level for initial ILD assessment in this model. The schematic representation of the dosing regimen used for initial ILD model development is shown in Fig. 1A. Fibrosis severity increased progressively with the number of T-Dxd doses, peaking after four weekly administrations (Group-1) (Fig. 1B) (Supplementary Table 2). Statistical analysis revealed significant increases in fibrosis scores in groups receiving three or four doses compared to trastuzumab controls at corresponding time points ($p < 0.01$). No significant fibrosis was observed in trastuzumab-treated animals across all dosing regimens. Histological distortion in T-Dxd-treated groups, characterized by alveolar septal thickening and fibrotic remodeling, while minimal to no pathological changes were observed in Trastuzumab-treated lungs (Fig. 1C). The observed histological features shown in Fig. 2B–J closely resemble those documented in clinical settings[6] and non-human primate studies[12], supporting the translational relevance of this model. Notably, lung injury emerged only after multiple doses, indicating that repeated ADC exposure rather than a single high dose is essential to trigger ILD-associated changes. Whether this reflects attainment of a critical pulmonary concentration, a time-dependent biological process, or both cannot be distinguished in the current study.

The histopathology scoring system enables a comprehensive evaluation of ADC-induced ILD

Initial high-dose T-Dxd studies showed that repeated administration generated a range of pulmonary findings, including alveolar septal thickening, inflammatory cell infiltration, edema, hemorrhage, and evolving fibrotic remodeling. These observations indicated that ILD-like injury in mice reflects a continuum of inflammatory and remodeling events rather than a single discrete lesion. Accordingly, a structured and semi-quantitative scoring approach was developed to capture the multifactorial nature of ADC-associated lung injury and to support consistent, reproducible assessment across studies. This framework complements conventional toxicology endpoints and facilitates early identification of potential ILD risk in ADC programs, an emerging priority for translational safety evaluation[15]. To capture this complexity, we systematically assessed pulmonary toxicity across treatment groups and implemented a 12-parameter histopathology scoring system (Fig. 2A) that captures hallmark pathological features reported in both clinical[16] and non-human primate studies of ADC-induced ILD[12]. The parameters, illustrated in Fig. 2A and exemplified in panels B–J, span the spectrum of ILD pathology from acute inflammatory changes (e.g., alveolar inflammation, granulomas, lymphocytic infiltration, and mononuclear cell infiltration) to vascular and interstitial alterations (perivascular/intravascular edema, hemorrhage, pulmonary congestion, and microthrombi) and chronic remodeling (peribronchial thickening, fibrin deposition, and pulmonary fibrosis). Each parameter was scored semi-quantitatively based on whole-slide image analysis of lung sections, allowing for reproducible and granular evaluation of lung injury across cohorts. ILD severity was scored on a scale of 0–3 based on estimated tissue involvement across the whole slide image (WSI). Scores reflected the extent of histopathological features, with 0 (Normal) ≦ 5%, 1 (Mild) = 5–33%, 2 (Moderate) (33–66%), and 3 (Marked) (>66%). The composite ILD severity score was derived by summing individual parameter scores. This structured scoring approach allowed clear discrimination between ADCs with low versus high pulmonary toxicity and demonstrated sensitivity to changes in dosing frequency.

Delayed onset of T-Dxd-induced interstitial fibrosis in the murine ILD model

The 200 mg/kg dose of T-Dxd was intentionally used as an initial dose-finding and feasibility study to establish whether ILD-like pulmonary pathology could be reproducibly induced in mice. After confirming the presence of ILD-like pathology under high-exposure conditions, we then refined the dosing regimen to more closely align with clinically relevant exposures to evaluate the sensitivity and translational applicability of the model. Recognizing that non-human primate (NHP) studies demonstrated delayed-onset ILD following repeated, clinically relevant T-Dxd exposure[12], we conducted a time-course study to characterize the temporal dynamics of pulmonary injury. To enhance translational relevance, the dose was reduced to 100 mg/kg, which approximates the human equivalent exposure range derived from the approved 5.4 – 8 mg/kg clinical dose when adjusted for species-specific pharmacokinetics[1]. This lower dose was selected to elicit ILD-like pathology while minimizing acute toxicity and enabling observation of delayed pulmonary effects.

Mice received T-Dxd or Trastuzumab at 100 mg/kg (Q3D), and lungs were evaluated at 48 h, 1 week, and 2 weeks post final dose (Fig. 3A). Mean injury scores for fibrosis (Fig. 3B), (Supplementary Table 3) are elevated in T-Dxd treated mice compared to Trastuzumab controls after 1 week and 2 weeks, with the highest score at 2 weeks. Composite injury scores (supplementary Fig. S1) revealed that T-Dxd induced a broad range of lesions, including alveolar septal thickening, inflammatory infiltrates, pneumocyte hyperplasia, and early fibrotic changes, each contributing to overall

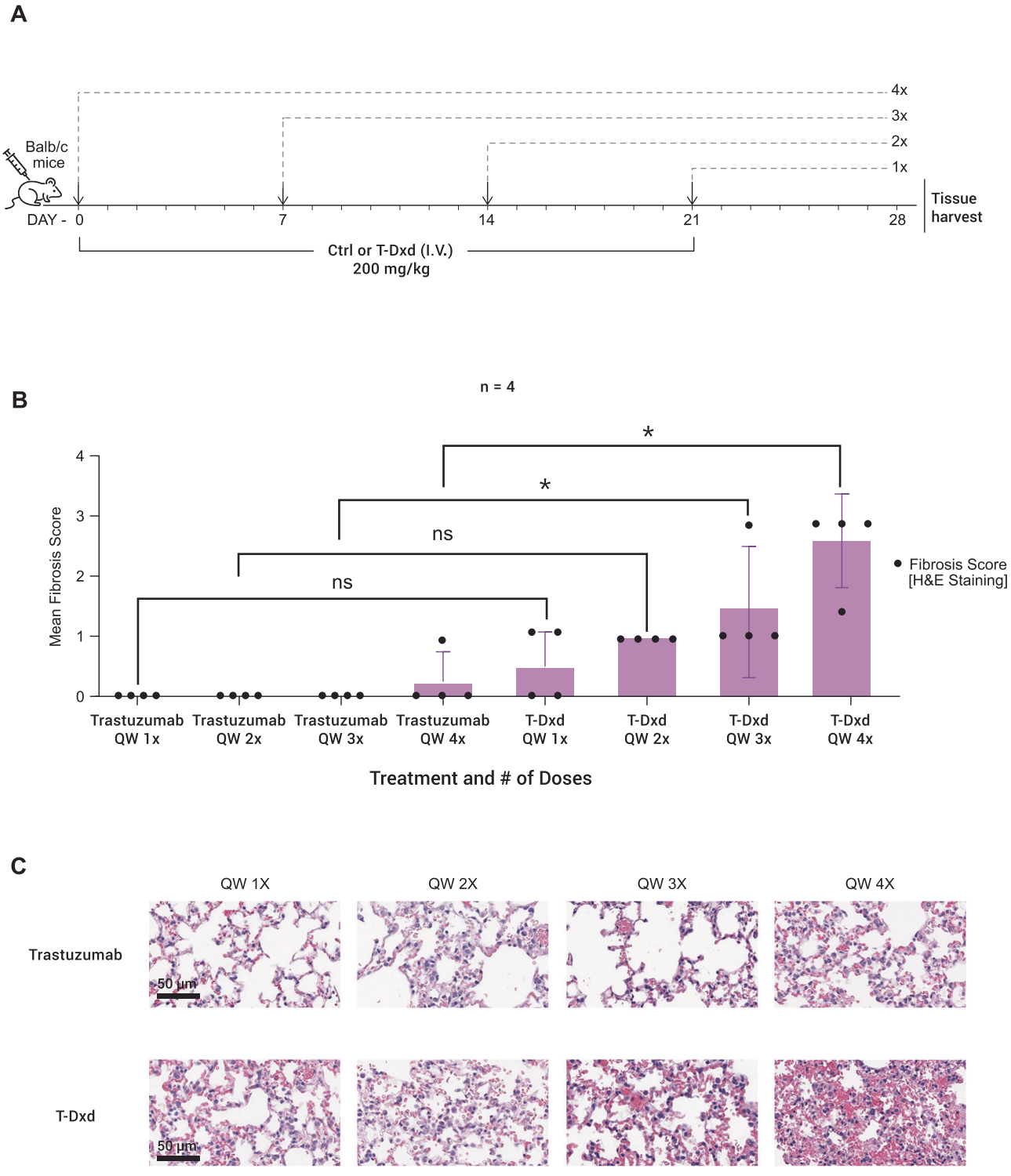

Fig. 1 | Dose-dependent induction of pulmonary fibrosis following repeated Trastuzumab deruxtecan dosing in mice. A Schematic of the weekly dosing regimen (QW 1× – 4×) for Trastuzumab deruxtecan (T-Dxd) and Trastuzumab control groups. **B** Mean fibrosis scores (mean ± SD) assessed by semi-quantitative histopathological grading. *$p < 0.05$, QW 3× and QW 4× vs. matched Trastuzumab treatment groups ($n = 4$). **C** Representative H&E-stained lung sections showing preserved alveolar architecture in Trastuzumab-treated mice and progressive alveolar septal thickening and fibrotic remodeling in Trastuzumab deruxtecan (T-Dxd) treated mice with increasing dose frequency. Scale bars represent 50 µm.

pathology severity. Trastuzumab-treated animals maintained low injury and composite scores throughout. Histological analysis (Fig. 3C) (supplementary Fig. S2) confirmed these quantitative findings. A representative whole-slide image is provided in Supplementary Fig. S3. At 1-week post-last dose, T-Dxd-treated lungs exhibited diffuse alveolar damage with interstitial widening and inflammatory cell infiltration. 2 weeks after the last dose, tissue architecture was distorted, with ongoing inflammation and fibrosis. In contrast, Trastuzumab controls showed preserved alveolar structure and minimal pathology at all time points. Our murine findings are consistent with non-human primate data, where cynomolgus monkeys given T-Dxd at ≥30 mg/kg every 3 weeks (4 doses) developed interstitial pneumonitis with lymphocytic infiltration, alveolar edema, and fibrosis[12]. The concordance

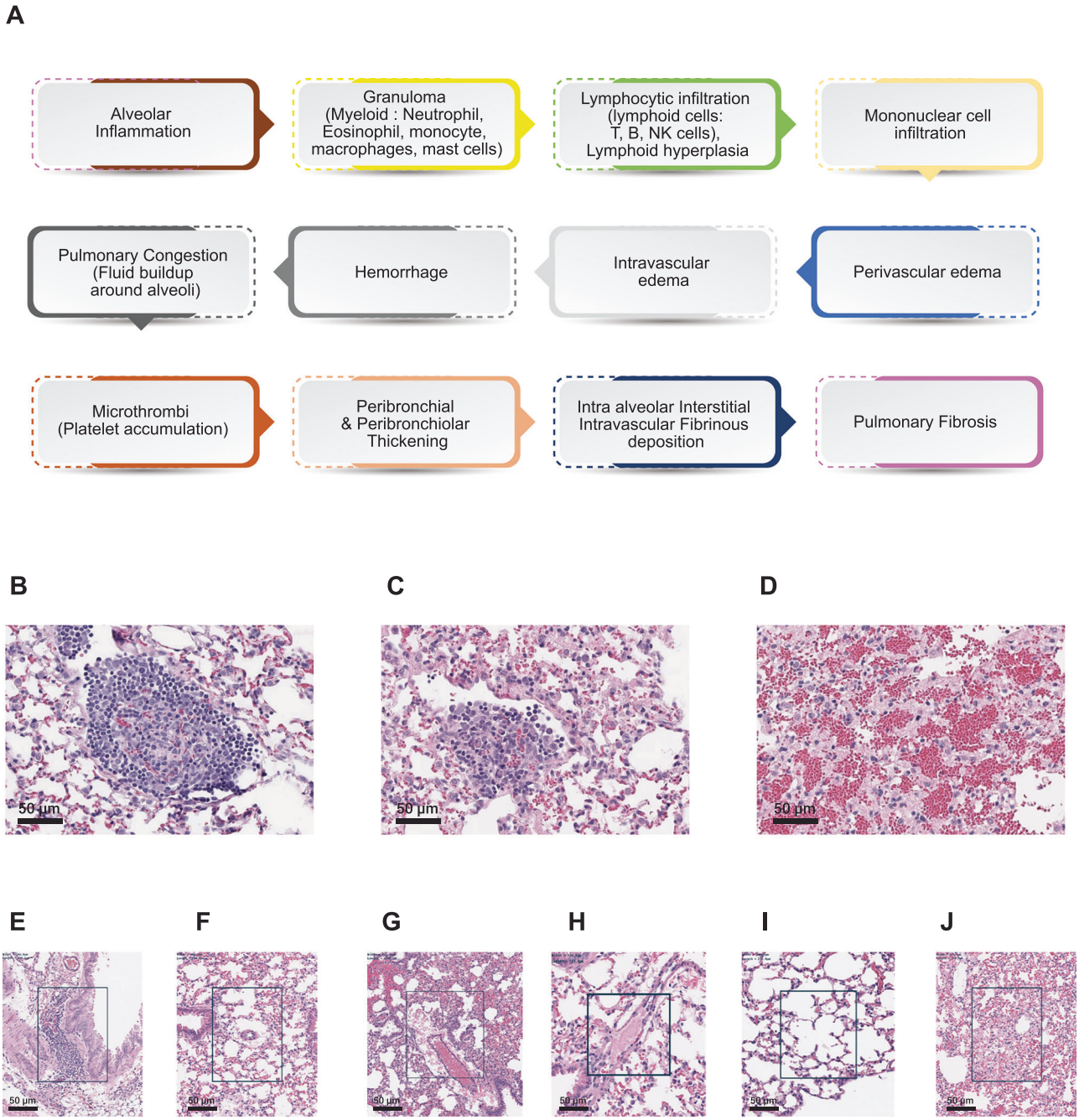

Fig. 2 | Twelve-parameter histopathology scoring system for ADC-induced ILD. **A** Schematic representation of the 12 histopathological parameters assessed in the ILD scoring system, arranged sequentially from acute inflammatory changes to chronic fibrotic remodeling. **B**–**J** H&E-stained lung histology images corresponding to key pathological parameters assessed in the study. **B** macrophage infiltration (Score 3). **C** Mono-nuclear cell infiltration (Score 2). **D** hemorrhage (Score 3). **E** Peribronchial inflammation (Score 2). **F** Perivascular edema (Score 2). **G** Perivascular edema with fluid expansion surrounding vessels. (Score 3). **H** Microthrombi within pulmonary vessels. (Score 2). **I** Fibrosis (Score 0). **J** Pulmonary fibrosis with thickened alveolar septa and collagen deposition (Score 3). All images are shown at 40× magnification, with scale bars indicating reference length (50 µm).

between murine and NHP temporal patterns highlights the model's translational utility for early detection of ADC-associated pulmonary risk.

Minimal lung toxicity observed with SN-38-based ADCs in pre-clinical ILD model

Previous time-course experiments demonstrated that ILD-like changes in mice were most consistently detectable approximately two weeks following the final ADC dose. Therefore, to evaluate ADC-induced lung injury, this interval was selected as the standardized observation window. We applied the same delayed-onset ILD assessment protocol to test ADC constructs. Mice were administered with ADCs at 100 mg/kg intravenously Q3D for 2 weeks (Fig. 4A). Study arms included Vehicle, Trastuzumab, T-SN-38-CL2A, and T-Dxd. Although pharmacokinetics is different between T-Dxd and SN-38-based ADCs, a uniform mg/kg dose (100 mg/kg) was used across groups to enable controlled cross-construct comparison. Lungs were collected 14 days after the final dose for histopathologic evaluation. Pulmonary pathology between T-Dxd and T-SN-38-CL2A treatment cohorts was compared under parallel dosing conditions. Mean injury scores for fibrosis, interstitial fibrinous deposition, hemorrhage, edema, and lymphocytic infiltration

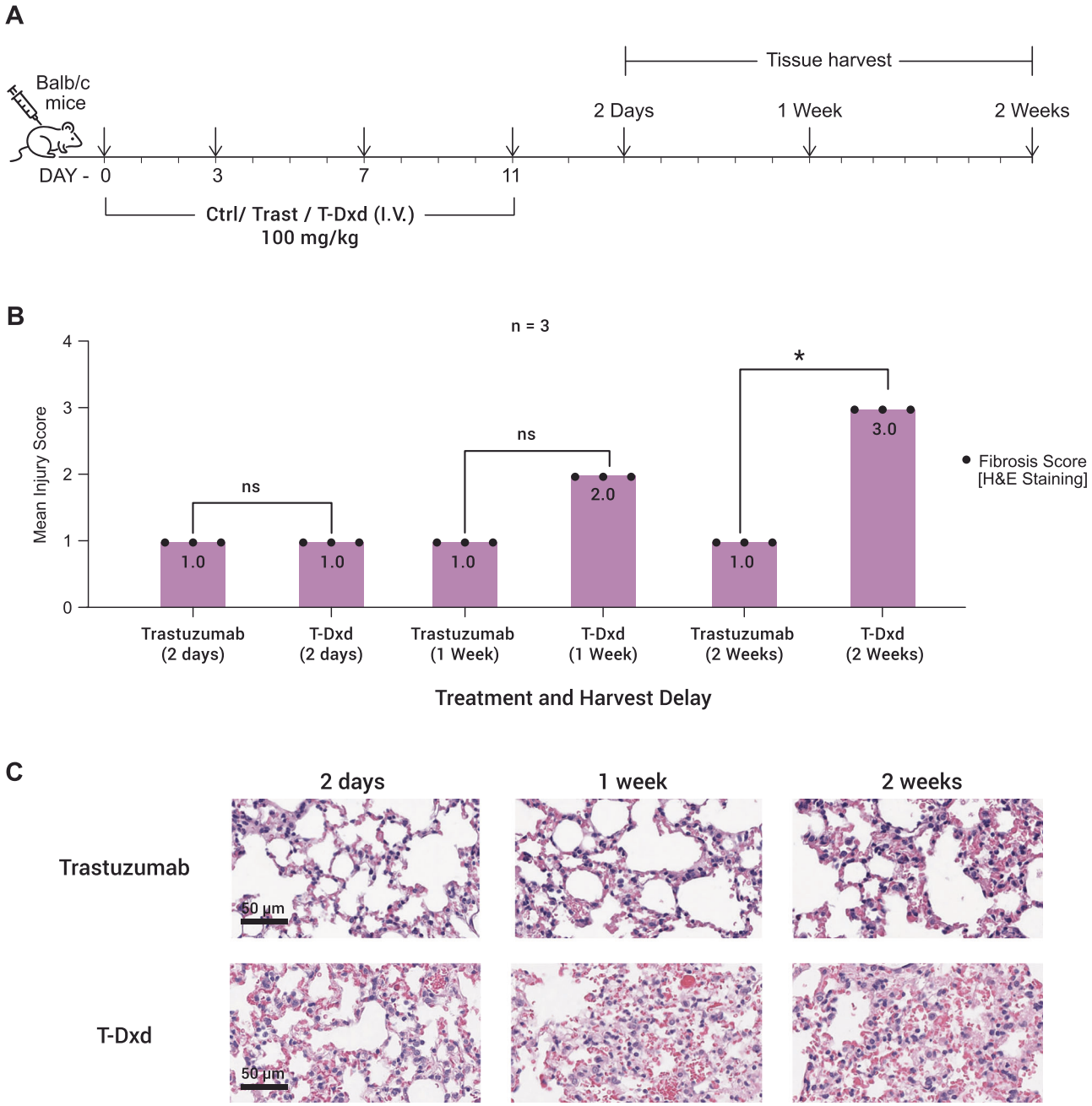

Fig. 3 | Time course study to assess lung injury following T-Dxd administration in mice. A Schematic of the dosing regimen and tissue collection schedule. Mice received repeated doses of Trastuzumab deruxtecan (T-Dxd), and lung tissues were harvested at 2 days, 1 week, and 2 weeks post-final dose for histopathological evaluation. **B** Quantification of lung injury severity expressed as mean fibrosis (injury) scores ±SD at each indicated time point. Scores were derived from blinded histopathological assessment using a composite lung injury scoring system, with increasing scores reflecting greater fibrotic involvement. **C** Representative hematoxylin and eosin (H&E) stained lung sections from T-Dxd treated and Trastuzumab-treated mice. At 1-week post-dose, T-Dxd-treated lungs show areas of persistent pneumocyte hyperplasia with focal interstitial fibrosis. At 2 weeks post-dose, sections demonstrate ongoing inflammatory infiltrates accompanied by architectural distortion of the alveolar spaces. In contrast, lungs from Trastuzumab-treated control mice exhibit preserved alveolar architecture with minimal inflammatory or fibrotic changes. Scale bars = 50 µm.

(Fig. 4B) and composite injury scores for several ILD parameters (Fig. 4C), (Supplementary Table 4) revealed no ILD-like pathology in Vehicle, Trastuzumab, and T-SN-38-CL2A-treated mice, with consistently low severity values across all 12 ILD parameters. Histopathological analysis two weeks post last dose confirmed preserved alveolar architecture in T-SN-38-CL2A treated lungs, with no evidence of peribronchial inflammation, septal thickening, or fibrotic remodeling, supporting their favorable lung safety-profile, even under conditions designed to uncover delayed-onset ILD (Fig. 4D). In contrast, T-Dxd treated mice exhibited markedly elevated composite and mean injury scores, reflecting a broad range of pathological features including alveolar septal thickening, inflammatory cell infiltration, pneumocyte hyperplasia, peribronchial inflammation, granuloma formation, and focal hemorrhage. These lesions were absent in all other treatment groups, highlighting a clear divergence in pulmonary outcomes between ADCs T-SN-38-CL2A and T-Dxd.

Together, these findings suggest that the pulmonary effects observed are not solely explained by topoisomerase-I inhibition from the ADC payload. While this data demonstrates that the model can distinguish ADCs with differing pulmonary responses, mechanistic conclusions regarding

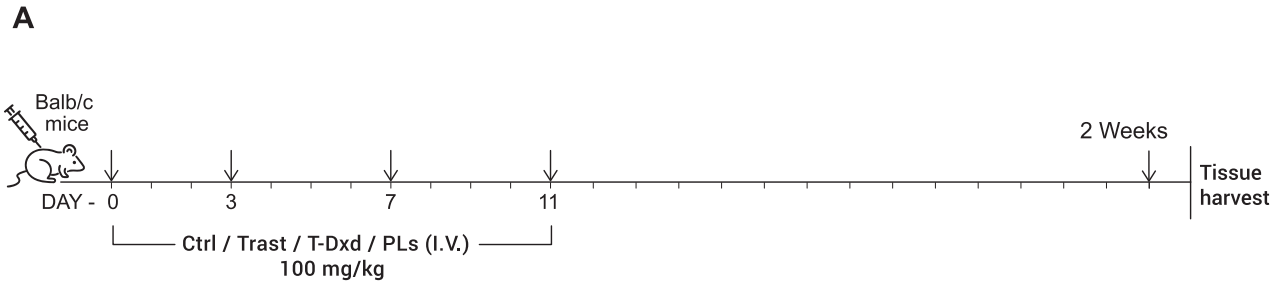

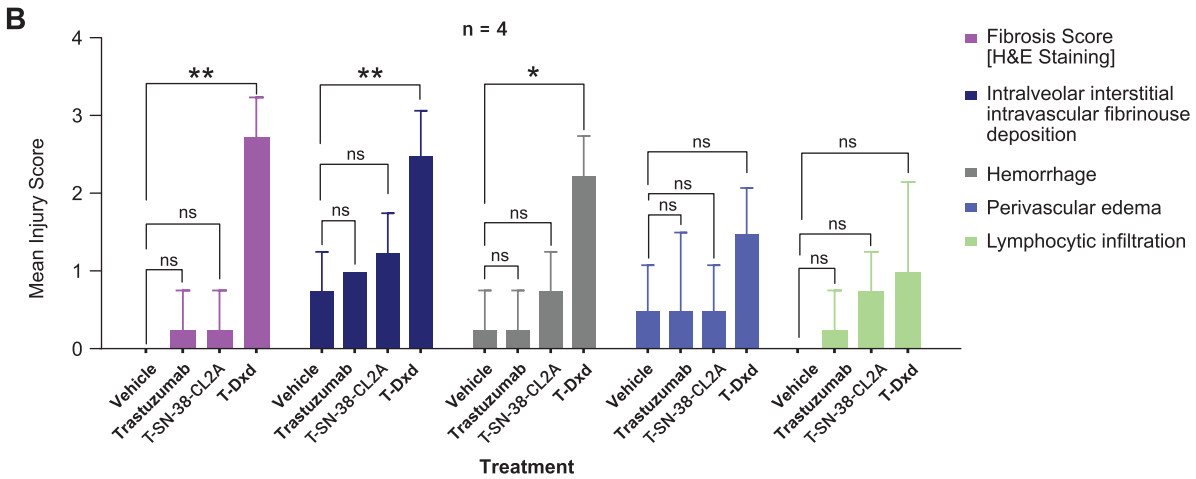

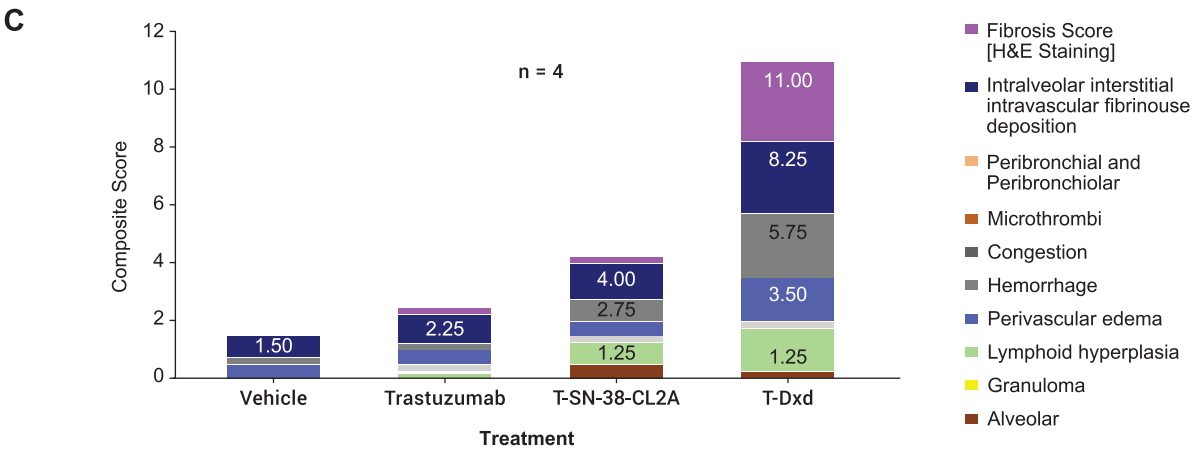

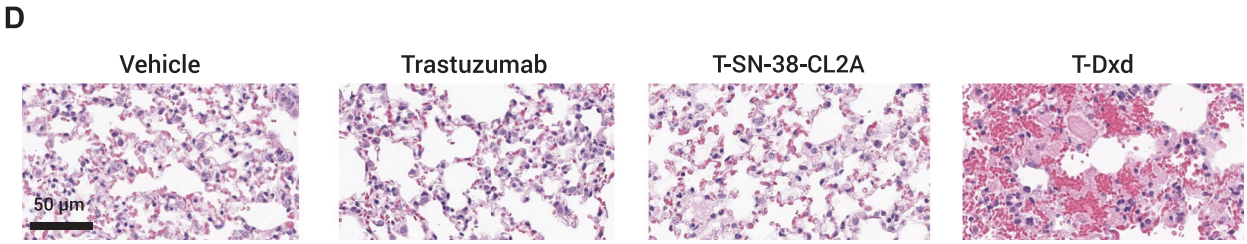

Fig. 4 | Comparison of SN-38 and Deruxtecan-based ADCs in the delayed-onset ILD murine model. A Schematic of the delayed onset ILD dosing regimen and study design. Mice were administered vehicle, unconjugated Trastuzumab, Trastuzumab-SN-38 conjugate with a CL2A linker (T-SN-38-CL2A), or Trastuzumab Deruxtecan (T-Dxd) according to the delayed onset protocol, followed by lung tissue collection at the terminal time point. **B** Quantitative histopathological assessment of individual lung injury parameters 2 weeks post-final dose, including fibrosis, interalveolar inflammation, interstitial inflammation, intravascular fibrinous deposition, hemorrhage, perivascular edema, and lymphocytic infiltration. Data are presented as mean ± SD, derived from blinded scoring of H&E-stained lung sections. **C** Composite lung injury scores (mean ± SD) calculated across 10 predefined ILD-associated histopathological parameters for Trastuzumab, T-SN-38-CL2A, and T-Dxd treatment groups. Composite scores reflect the aggregate severity of lung injury features assessed at the study endpoint. **D** Representative hematoxylin and eosin (H&E) stained lung sections from each treatment group. Vehicle, Trastuzumab, and T-SN-38-CL2A-treated mice show preserved alveolar architecture with minimal inflammatory or fibrotic changes. In contrast, lungs from T-Dxd-treated mice exhibit extensive ILD-like lesions characterized by inflammatory infiltrates, alveolar wall thickening, and architectural distortion. Scale bars = 50 µm.

specific structural drivers cannot be inferred from this comparison alone. SN-38 and Dxd differ in potency, biodistribution, and pharmacologic properties, and therefore direct attribution of the observed differences to linker or payload components is not appropriate. Instead, these results highlight the capability of this model to detect ADCs with differential pulmonary safety profiles and support future mechanistic work using matched payload-linker constructs to define structural contributors to ILD risk more precisely.

Evaluation of structural features contributing to ADC-associated ILD

ADC-induced interstitial lung disease (ILD) is thought to arise, at least in part, from dose-dependent but target antigen-independent uptake of ADCs in lung tissue via Fcγ receptor-mediated internalization by alveolar macrophages[17]. We hypothesized that structural elements of ADCs, including linker design, molecular architecture, and physicochemical properties, may modulate target-independent pulmonary uptake and/or local payload release, thereby contributing to ILD liability. Similar considerations regarding the role of ADC architecture in pulmonary toxicity have recently been proposed in the context of CEACAM5-exatecan ADC development by Sloot et al.[13]. To explore whether the murine ILD model could differentiate pulmonary responses across ADC constructs with distinct architectures, we generated an exploratory ADC incorporating the same GGFG (Gly-Gly-Phe-Gly) cleavable sequence and immolation motif used in T-Dxd but replacing the cytotoxic payload with a non-cytotoxic cyclohexylamine ("dummy" payload). This construct T-MC-GGFG-Cy (structure shown in Table 1) was synthesized to enable evaluation of structural contributions under otherwise comparable dosing conditions. A dose response viability assay showed that both the Trastuzumab-dummy payload ADC (T-MC-GGFG-Cy) and unconjugated Trastuzumab produced comparable effects on cell viability, with overlapping concentration response profiles, confirming that the dummy payload did not contribute to the cytotoxicity (Fig. 5B). The cytotoxicity profiles were independently confirmed using a confluence-based proliferation assay measured with the Incucyte S3 live-cell imaging platform. Representative data are shown in Supplementary Fig. S4. We then compared lung injury induced by T-MC-GGFG-Cy, T-Dxd, Trastuzumab, and vehicle controls using our delayed-onset ILD assessment protocol (Fig. 5A). All groups were dosed under identical schedules and comparable mg/kg exposures. The mean injury scores revealed substantial differences in ILD severity between the treatment groups. Both ADCs with cleavable peptide linkers with specific chemical motifs, such as the GGFG (T-Dxd and T-MC-GGFG-Cy), induced pronounced pulmonary pathology, including lymphocytic infiltration, perivascular edema, hemorrhage, and fibrosis (Fig. 5C). Importantly, these differences were independent of the presence of cytotoxic payload, as observed with ADC containing a non-cytotoxic dummy payload. The composite lung injury scores in mice treated with T-MC-GGFG-Cy approached those of T-Dxd and were significantly higher than Trastuzumab or vehicle controls ($p < 0.01$) (Fig. 5D), (Supplementary Table 5). Histopathology assessment (Fig. 5E) revealed that Vehicle and Trastuzumab-treated lungs preserved alveolar architecture with no significant lesions. In contrast, T-MC-GGFG-Cy-treated lungs exhibited ILD-like changes, including alveolar wall thickening, interstitial inflammatory infiltrates, and fibrotic foci. T-Dxd-treated lungs showed a comparable ILD injury pattern with hemorrhage and diffuse parenchymal remodeling. The observed ILD pathology between T-Dxd-based ADCs and T-SN-38-CL2A confirms that the ADCs carrying the same cytotoxic payload class but conjugated through different linkers yielded divergent outcomes, with non-GGFG linker architectures producing minimal lung injury.

Evaluation of linker–payload engineered ADC variants with preserved antitumor activity and markedly reduced ILD liability

Motivated by prior observations that a GGFG-linked dummy payload elicited pronounced ILD features relative to T-Dxd, we sought to determine whether modifying linker–payload architecture could mitigate ADC-associated pulmonary injury without compromising antitumor activity. To this end, we applied a stepwise evaluation strategy using our delayed-onset ILD protocol to assess four novel ADCs: NJB-T-PL10, NJB-T-PL30, NJB-T-PL90, and NJB-T-PL119 (Table 2). We initially generated and evaluated NJB-T-PL10 and NJB-T-PL30, both of which incorporate a GGFG-based cleavable linker but differ in their topoisomerase I inhibitor payloads. In efficacy studies using the JIMT-1 xenograft model, both NJB-T-PL10 and NJB-T-PL30 demonstrated measurable antitumor activity (Fig. 6A). However, NJB-T-PL10 exhibited reduced efficacy compared with NJB-T-PL30. Despite these differences in efficacy, both constructs produced consistently elevated composite ILD scores under the delayed-onset protocol, reflecting increased fibrosis, interalveolar and interstitial inflammation, intravascular fibrinous deposition, peribronchial and peribronchiolar inflammation, microthrombi, vascular congestion, hemorrhage, perivascular edema, lymphoid hyperplasia, granulomatous changes, and alveolar injury relative to vehicle and Trastuzumab-treated controls (Fig. 6D, E), (Supplementary Table 6). These findings indicate that ILD liability is retained across different payloads with a shared GGFG linker and immolation motif. Next, to assess whether altering linker–payload architectural features could modulate this phenotype, we synthesized NJB-T-PL90, in which the NJB-T-PL30 payload was preserved while the GGFG linker was replaced with a non-GGFG linker. This novel ADC variant showed tumor efficacy comparable to T-Dxd (Fig. 6B) and showed reduction in composite ILD scores approaching levels observed in vehicle and Trastuzumab treatment groups (Fig. 6F), suggesting attenuation of lung injury with changes in linker–payload architecture. To further extend this observation, we generated NJB-T-PL119, which retained the same non-GGFG linker used in NJB-T-PL90 but incorporated a structurally distinct topoisomerase I inhibitor payload. The resulting ADC, NJB-T-PL119, showed significant efficacy against JIMT-1 tumors (Fig. 6C) and exhibited the lowest composite ILD scores among the tested ADCs, with minimal histopathologic features of lung injury (Fig. 6G). All four novel ADC variants demonstrated tumor growth inhibition, indicating that the observed ILD scores were not associated with a loss of antitumor activity. Collectively, these findings provide preliminary evidence that ADC linker–payload architecture is associated with differences in ILD liability, with GGFG-based cleavable constructs showing higher composite lung injury scores and non-cleavable architectures showing reduced pathology in our ILD model.

While these exploratory observations raise the possibility that ADC structural features may influence ILD-like outcomes, definitive attribution of lung toxicity to any specific component (e.g., linker structure, payload class, or other molecular properties) requires further mechanistic investigation. Construct-matched controls (e.g., an exatecan-based ADC with a CL2A linker) and dedicated pharmacokinetic and tissue-distribution analyses will be needed to precisely dissect structure-toxicity relationships, which are beyond the scope of the present study. However, the data indicate that modifying the nature of the linker, immolation motif, and payload is key to attenuating off-target activity in the lung while preserving antitumor potency.

Discussion

In this study, we established a cost-effective and reproducible murine model for evaluating ADC-induced interstitial lung disease, with a focus on recapitulating the pulmonary toxicity observed in clinical settings. Currently, non-human primate models are the primary in vivo systems used to assess ADC-related ILD. However, these models are limited by cost, ethical constraints, and low throughput. Our murine platform provides a valuable alternative for early-stage screening, enabling rapid and scalable evaluation of ADC candidates. We chose female BALB/c mice for initial model establishment to reduce inter-animal variability and minimize stress-related inflammatory effects that can occur with male group housing in repeated-dose studies. Evaluation of sex- and strain-dependent differences in susceptibility to lung toxicity will be addressed in future studies.

The histopathological features, alveolar inflammation, interstitial thickening, and delayed fibrotic changes observed in our ILD model closely

Table 1 | Test articles evaluated in studies

ADC#	Ab- [Chemical structure] DAR ADC name
1	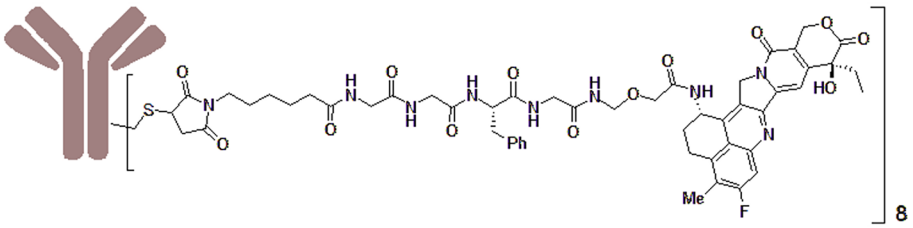 **T-Deruxtecan**
2	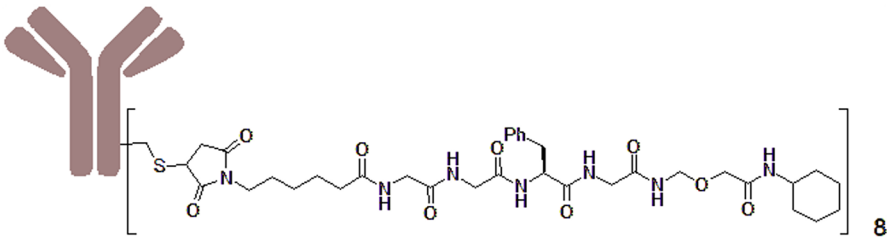 **T-MC-GGFG-Cy**
3	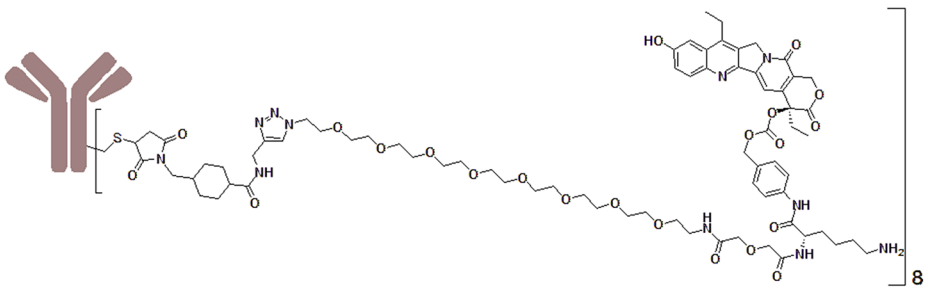 **T-SN38-CL2A**

Test articles evaluated in this study.
Schematic representation of antibody–drug conjugates (ADCs) used in the study, showing antibody scaffold, linker, and payload structures. The drug-to-antibody ratio (DAR) was fixed at 8.

align with clinical observations reported in patients treated with T-Dxd[18,19]. In a post-marketing surveillance study of T-Dxd-associated ILD/pneumonitis, diffuse alveolar damage (DAD) was found to be associated with the most fatal cases (72.7%, 8/11)[20]. Our ILD model captures key pathological features of DAD relevant to severe ADC-associated lung injury. Notably, we demonstrate that ILD in this model emerges in a delayed fashion, with minimal pathological findings at 48 h and 1-week post-final dose, but clearly defined ILD lesions by 2 weeks. This delayed onset mirrors findings in both NHP studies and pooled clinical trial data, where the median time to ILD onset ranged from 2 to 6 months[6,12]. These findings underscore the importance of extending observation windows in preclinical toxicity studies to capture the full spectrum of pulmonary adverse events. Moreover, susceptibility to drug-induced ILD may be influenced by genetic variability, as some individuals exhibit higher sensitivity to certain anticancer drugs due to their genetic background or pre-existing pulmonary conditions[21,22]. While it is challenging to investigate this hypothesis in non-human primates, murine models provide a feasible alternative for evaluating genetic contributions to ILD risk.

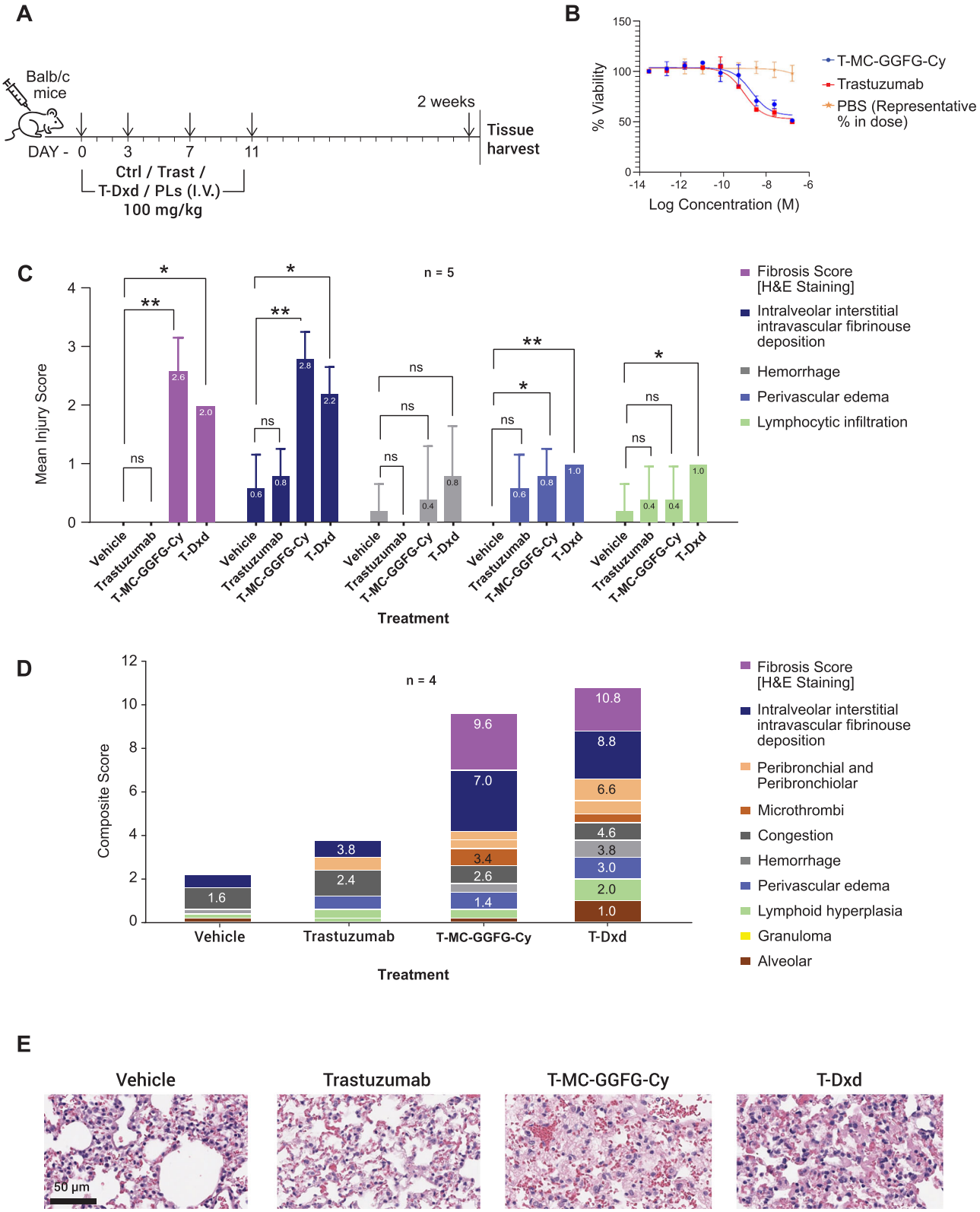

Although advanced histochemical stains, such as Masson's trichrome to detect pulmonary fibrosis or immunohistochemistry for immune markers (e.g., CD68 and CD3), could offer additional insight into fibrotic remodeling and immune cell recruitment, our pulmonary findings reflected a mixed interstitial lung disease like injury, including inflammatory alveolitis, interstitial pneumonitis, vascular injury, and remodeling changes, with collagen deposition observed only in a subset of animals. Therefore, H&E staining was used as the primary basis for standardized histopathologic assessment across all evaluated parameters to maintain consistency and comparability. This supports the feasibility of a streamlined, reproducible workflow for early toxicity screening.

When evaluated under matched conditions, T-Dxd produced ILD-like pathology, whereas the SN-38-based ADC T-SN-38-CL2A did not. These findings are consistent with clinical observations that ILD risk has not been

Fig. 5 | Linker payload architecture drives ADC-associated ILD in the delayed-onset murine model. A Delayed onset dosing scheme for vehicle, Trastuzumab, T-MC-GGFG-Cy (dummy payload linker conjugate), and T-Dxd. **B** In-vitro cytotoxicity of Trastuzumab and T-MC-GGFG-Cy ADC constructs. HER2$^+$ SK-BR-3 cells were treated with increasing concentrations of Trastuzumab or the non-cytotoxic control conjugate T-GGFG-Cy for 72 h. Cell viability was assessed using the CellTiter-Glo assay and normalized to untreated controls. Both Trastuzumab and T-MC-GGFG-Cy showed comparable dose response profiles across all concentrations (M), confirming preserved antibody binding and the lack of additional cytotoxicity by the T-MC-GGFG-Cy construct. Data represent mean ± SD of triplicate wells. **C** Mean injury scores (mean ± SD) of fibrosis, interalveolar, interstitial, and intravascular fibrinous deposition, highlighting elevated pathology in T-MC-GGFG-Cy and T-Dxd groups compared to Trastuzumab and vehicle controls. **D** Composite injury scores (mean ± SD) across 10 ILD parameters for Trastuzumab, T-GGFG-Cy, and T-Dxd treatment groups. **E** Representative H&E lung sections showing preserved alveolar structure in vehicle and Trastuzumab groups and marked fibrotic foci in T-MC-GGFG-Cy and T-Dxd treated lungs. Scale bars = 50 μm.

associated with SN-38-containing ADCs to date. However, SN-38 and Dxd differ in pharmacology, potency, membrane permeability, and bystander effects, making direct attribution of injury to any single structural component inappropriate. Finally, the inclusion of NJB-T-PL119, a Trastuzumab-based ADC incorporating an alternative non-GGFG linker, provided an additional functional readout of the model's discriminatory capacity. Under identical dosing conditions, NJB-T-PL119 demonstrated antitumor efficacy comparable to T-Dxd in the JIMT-1 xenograft model yet produced only minimal lung injury in the ILD system. The marked separation in pulmonary responses between NJB-T-PL119 and T-Dxd, despite their shared antibody and payload class, supports the concept that linker architecture can influence the balance between efficacy and pulmonary safety. Our findings provide proof-of-concept that linker engineering can modulate ILD outcomes and demonstrate that highly active HER2-targeted ADCs can be designed with significantly reduced pulmonary liability. While further mechanistic studies, particularly using fully matched constructs, are required to define the precise determinants of this difference, NJB-T-PL119 serves as a practical demonstration of how this model can be used to evaluate next-generation ADCs engineered to minimize ILD risk.

Taken together, these results support the utility of this murine platform for early triage of ADC candidates with potential ILD liability. The model recapitulates clinically relevant delayed-onset lung injury, discriminates between constructs under matched conditions, and can serve as a translational bridge prior to NHP studies. Future work will focus on incorporating mechanistic analyses, structurally matched ADC comparators, and extended endpoints, which will further refine the understanding of ADC-associated lung injury and strengthen predictive accuracy.

In summary, this work establishes a practical and reproducible murine model that recapitulates delayed-onset, ADC-associated ILD, consistent with clinical and NHP observations. The model enables discrimination of differential pulmonary responses among ADC constructs under matched conditions and supports the need for extended monitoring periods in preclinical safety studies. Alternatively, to histopathology and immunohistochemistry, Bronchoalveolar Lavage Fluid (BALF) analysis, along with Aashcroft scoring, would provide complementary information, particularly for distinguishing inflammatory pneumonitis from subsequent tissue remodeling or fibrotic change[23,24]. Our results indicate that this platform will serve as an early risk-stratification tool to identify ADC candidates that warrant closer toxicological evaluation during development, rather than a direct predictor of clinical toxicity. While exploratory comparisons revealed construct-dependent differences, definitive mechanistic attribution will require structure-matched controls and pharmacologic studies.

Methods

Test articles

The purchased reagents were used as is without further purification. Deruxtecan and CL2A-SN-38 were purchased from Medchem Express. Deuterated solvents were purchased from Cambridge Isotope Laboratories (Andover, MA). NMR spectra were recorded on a Varian Unity INOVA 500, and samples calibrated for: ^{1}H NMR (DMSO, $\delta = 2.5$ ppm). Trastuzumab (anti-HER2) (T) was purchased from Selleckchem (Cat. No. A2007, Selleckchem, Houston, TX). Novel ADCs NJB-T-PL10 and NJB-T-PL30 were synthesized according to methods disclosed in a published patent (WO2024/248944 A1). ADCs NJB-T-PL90 and NJB-T-PL119 were synthesized according to methods disclosed in a published patent (WO2025/222127 A2). ADCs T-Dxd, T-SN-38-CL2A, and T-MC-GGFG-Cy were prepared in 1× histidine buffer.

Antibody–drug conjugation

Trastuzumab at a concentration of 5.1 mg/mL was fully reduced using 9–12 molar equivalents of TCEP, followed by the addition of 12–13 molar equivalents of linker–payload in 10–20% v/v dimethylacetamide (DMA). The resulting conjugates were purified by size-exclusion chromatography and/or tangential flow filtration (TFF) into 20 mM histidine buffer (pH 5.5) over 6–10 diavolumes. The final conjugates were concentrated, sterile filtered through a 0.2 μm PTFE filter, and stored at the working concentration (Supplementary Table 1). The monomer content was confirmed by SEC using a TSKgel G3000SWXL column (7.8 × 300 mm). DAR was verified by LC-MS using a Waters Xevo G2-XS QTof mass spectrometer coupled to an ACQUITY UPLC system with a PLRP-S column (1000 Å, 8 μm, 2.1 × 50 mm). Chemical structures of the linker payloads used for conjugation are shown in Tables 1 and 2.

Cell viability assays

HER2-positive SKBR-3 breast cancer cells (ATCC HTB-30) were cultured in McCoy's 5A medium supplemented with 10% FBS at 37 °C with 5% CO_2. For the cytotoxicity assay, Cells were seeded in 96-well plates at 2×10^3 cells/well and allowed to adhere overnight. Serial dilutions of test articles (PBS Vehicle, Trastuzumab, and T-MC-GGFG-Cy) were prepared in assay medium (final concentration range: $2.5 \times 10^{-14} - 1.4 \times 10^{-7}$ M). Cells were treated for 144 h, after which viability was assessed using CellTiter-Glo® (Promega) according to the manufacturer's protocol. Luminescence was measured on a BioTek Synergy HTX plate reader. Curves were generated with a three-parameter nonlinear regression model in GraphPad Prism (v10). Data represent mean ± SD of triplicate wells. For confluence measurement, cells were treated in 96-well plates and placed in an Incucyte S3 live-cell imaging system and imaged every 12 h. Images were acquired using a 10× objective, capturing five fields per well. Cell confluence was quantified using Incucyte software (version 2024B) with the AI-Confluence analysis module. A size filter was applied to include objects larger than 500 μm² to exclude dead cells and debris. Confluence values were normalized to the baseline measurement at time 0. Data from the 144 h time point were exported and plotted against treatment concentration in GraphPad Prism (v10 or later). Curves were generated using a three-parameter nonlinear regression model.

Animal studies

All animal experiments were performed in compliance with institutional guidelines, approved by the Stony Brook University Institutional Animal Care and Use Committee (IACUC) (Protocol #2021-00074) and conducted in accordance with institutional guidelines and Code of Federal Regulations 9 CFR 2.31. Female Balb/C (RRID:MGI:2161072) mice 6–8 weeks (about 2 months) old were purchased from Taconic Biosciences (Germantown, NY). The mice were acclimated for at least 7 days prior to study initiation and housed under specific pathogen-free conditions with a 12-hour light/dark cycle, ad libitum access to food and water, and environmental enrichment. For initial ILD model development, Trastuzumab and T-Dxd

Table 2 | Novel ADCs evaluated in this study

ADC#	Ab- [Chemical structure] DAR ADC name
1	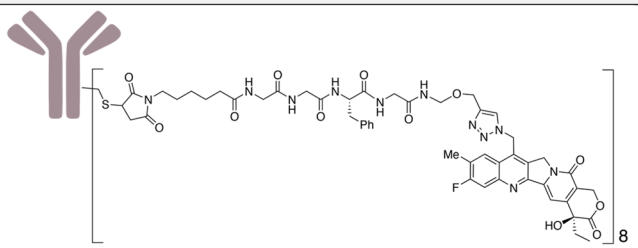 **NJB-T-PL10**
2	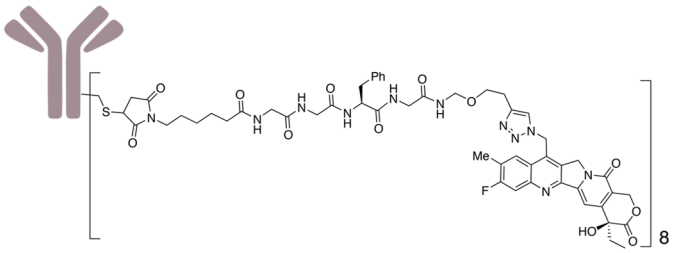 **NJB-T-PL30**
3	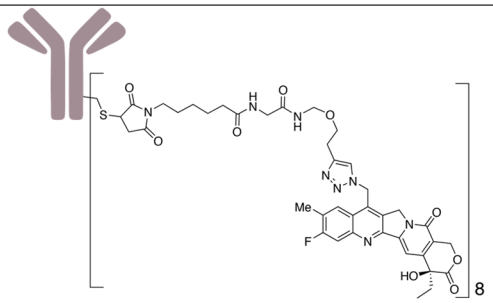 **NJB-T-PL90**
4	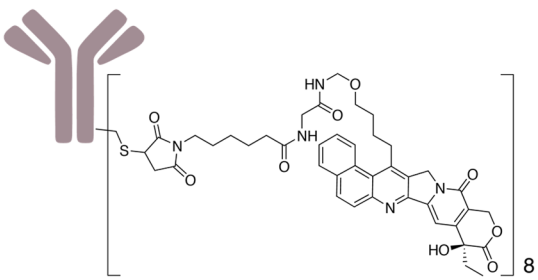 **NJB-T-PL119**

Schematic representation of the four HER2-targeted ADCs evaluated in this study.
NJB-T-PL10, NJB-T-PL30, NJB-T-PL90, and NJB-T-PL119, highlighting differences in linker–payload architecture. NJB-T-PL10 and NJB-T-PL30 incorporate a cleavable MC-GGFG linker, whereas NJB-T-PL90 and NJB-T-PL119 utilize non-cleavable, non-GGFG linker architectures.

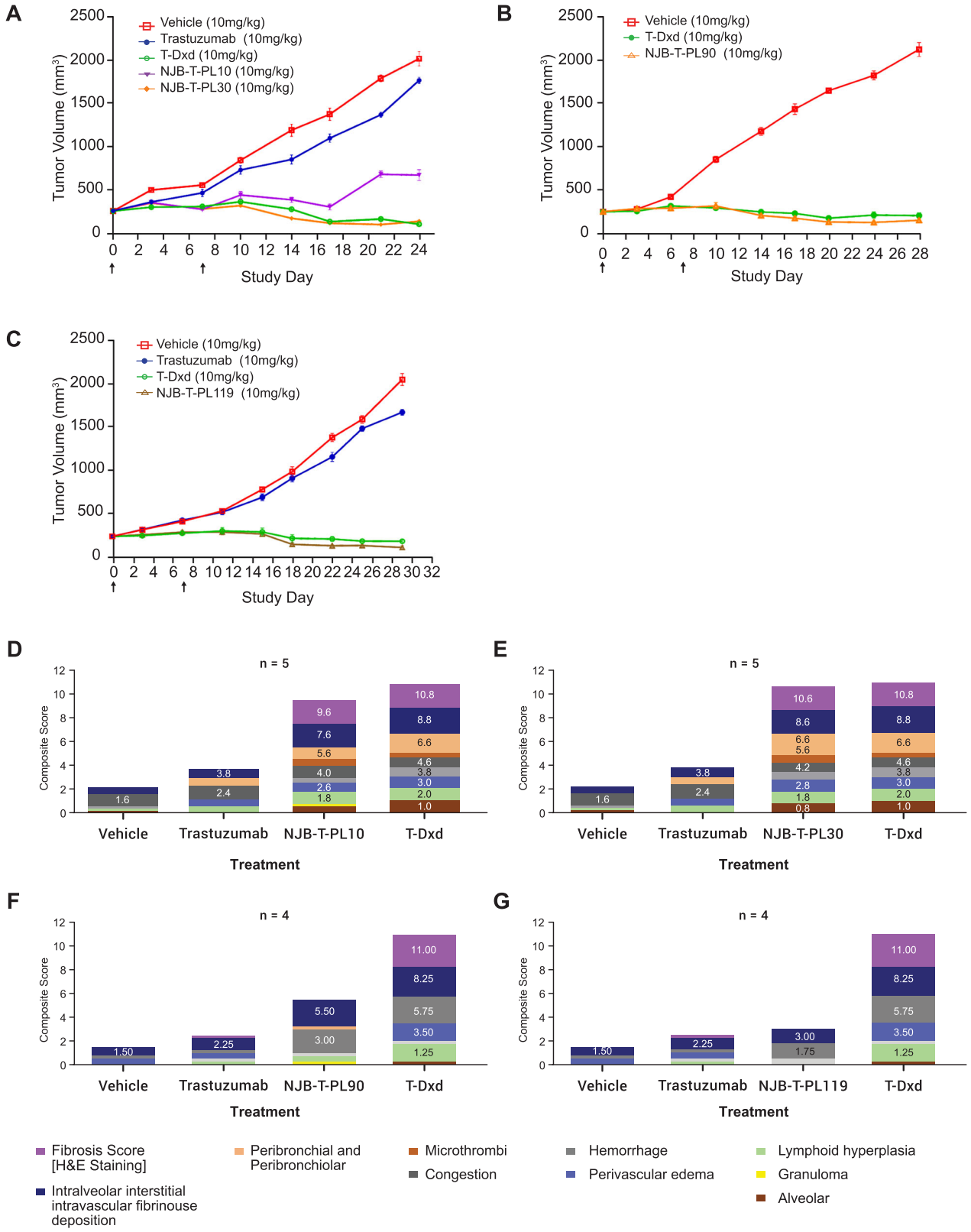

were administered at 200 mg/kg (5 mL/kg) once weekly for 4 weeks. Mice were assigned to four staggered dosing cohorts and administered intravenous doses on Days 0, 7, 14, and 21. Group 1 received doses on Days 0, 7, 14, and 21 (four doses total), Group 2 on Days 7, 14, and 21 (three doses), Group 3 received doses on Days 14 and 21 (two doses), and Group 4 received a single dose on Day 21 (Fig. 1A). All animals were euthanized on Study Day 28, by exposure to carbon dioxide gas in a rising concentration, followed by cervical dislocation to enable uniform histopathological assessment across groups and evaluate ILD-like changes as a function of repeated dosing. As a vehicle, 1× PBS pH 7.0, or HBS buffer (10 mM Histidine, 10% Trehalose, 0.02% Polysorbate 20, pH 5.5) was administered at the same volume as the ADCs. For the delayed ILD-onset protocol, the animals were randomized

Fig. 6 | Evaluation of linker–payload architecture on ILD liability while preserving antitumor activity using a delayed-onset ILD model. A–C Antitumor efficacy of NJB-T-PL10, NJB-T-PL30, NJB-T-PL90, and NJB-T-PL119, respectively, in the JIMT-1 xenograft model. Tumor growth inhibition was comparable to Trastuzumab deruxtecan (T-Dxd), indicating preserved antitumor activity across linker–payload designs. **D**, **E** Composite ILD scores following evaluation using the delayed-onset murine ILD protocol for NJB-T-PL10 (**D**) and NJB-T-PL30 (**E**) ($n = 5$ animals per group). **F**, **G** Composite ILD scores for NJB-T-PL90 (**F**) and NJB-T-PL119 (**G**) ($n = 4$ animals per group). Composite ILD scores reflect semi-quantitative histopathologic assessment of lung injury features, including fibrosis, intralveolar and interstitial inflammation, intravascular fibrinous deposition, peribronchial and peribronchiolar inflammation, microthrombi, vascular congestion, hemorrhage, perivascular edema, lymphoid hyperplasia, granulomatous changes, and alveolar injury. ADCs incorporating cleavable GGFG-based linkers (NJB-T-PL10 and NJB-T-PL30) exhibited elevated composite ILD scores comparable to T-Dxd, whereas non-GGFG linker architectures (NJB-T-PL90 and NJB-T-PL119) demonstrated reduced pulmonary pathology despite maintained antitumor efficacy.

into treatment groups based on body weight. The test articles T (Trastuzumab) and ADCs T-Dxd, T-SN-38-CL2A, T-MC-GGFG-Cy, NJB-T-PL10, NJB-T-PL30, NJB-T-PL90, and NJB-T-PL119 were administered intravenously at 100 mg/kg on a Q3D schedule for two weeks. A maximum of four doses was administered at three-day intervals, unless otherwise specified. Body weights and clinical signs were monitored at regular intervals to assess tolerability and systemic toxicity. Animals were euthanized two weeks post last dose or earlier if humane endpoint criteria were met.

Tumor efficacy studies

Female NOD.CB17-Prkdc<scid > /J (NOD-SCID) mice were purchased from Jackson Laboratory (Bar Harbor, Maine, USA). The mice were acclimated prior to study initiation and housed under specific pathogen-free conditions with a 12 h light/dark cycle, ad libitum access to food and water. JIMT-1 human breast cancer cells (ACC 589, DSMZ cell lines bank, Germany) cultured in 90% DMEM + 10% Hi FBS were harvested during logarithmic growth, counted, and resuspended in sterile PBS (+Matrigel, 1:1) at a final concentration of 3×10^7 cells/mL. Mice were inoculated subcutaneously in the right flank with 3×10^6 JIMT-1 cells in a total volume of 100 µL per mouse. For all in vivo tumor studies, power calculation to determine sample sizes (5% significance, 90% statistical power) is based on a two-tailed, Mann–Whitney *U* test. Stratified randomization has been performed for all efficacy studies. An independent researcher was assigned to blindly measure parameters such as tumor size to reduce or eliminate some sources of experimental bias. Tumor growth was monitored using digital calipers, and tumor volume (TV) was calculated using the formula $TV = (\text{length} \times \text{width}^2)/2$. Once tumors reached the predetermined enrollment range (typically ~200–250 mm^3), mice were randomized into treatment groups to ensure comparable mean tumor volumes at baseline. The test ADCs were administered at a dose of 10 mg/kg, given once weekly for 2 weeks (Q7D × 2) by intravenous injection. Control animals received Vehicle and/or Trastuzumab according to the same schedule. Tumor measurements and body weights were recorded at least twice a week throughout the study. Animals were monitored daily for clinical signs of distress, and predefined humane endpoints (maximum tumor volume or health criteria) were applied in accordance with institutional animal care and use committee (IACUC) approved protocols. Tumor growth inhibition and response rates were calculated relative to baseline and vehicle-treated controls.

Pathology and histological evaluation

At necropsy, lungs were inflated via the trachea with 1 mL of 10% neutral buffered formalin (NBF) using a 3 mL syringe fitted with a 27-gauge needle to preserve alveolar architecture. The tissues were immersion-fixed for 48 h at room temperature and then transferred to 70% ethanol for storage prior to processing. Whole lungs, including both left and right lobes, were processed and sectioned at 5µm thickness, placed on a glass slide, and then stained with hematoxylin and eosin (H&E) using standard protocols. For each animal, the entire lung section slides were digitally scanned using Aperio AT2 (MTC) or GT450 (H&E) scanner (Leica Biosystems, Inc.) to generate Whole Slide Images (WSIs), which were uploaded to the cloud platform for evaluation. Histopathologic evaluation was performed on the full cross-sectional area of the lung section, allowing assessment of all lobes present within the section and minimizing regional sampling bias. Lesions were scored semi-quantitatively across the entire lung section under blinded conditions. WSIs were reviewed in their entirety by a senior board-certified veterinary pathologist in a blinded manner. Previously annotated slides, Excel datasets, and pathology reports were reviewed and correlated with current findings. Interstitial lung disease (ILD)-like changes were scored using a semi-quantitative system based on published criteria[25,26]. Composite grading incorporated key pathological features, including alveolar septal thickening, inflammatory cell infiltration, pneumocyte hyperplasia, and fibrosis, with severity defined on a 3-point scale. Representative lesions were imaged under brightfield microscopy, and high-resolution, non-compressed images suitable for publication were acquired at 40 × magnification with a 50 µm scale bar. For archival and data sharing, images were uploaded to a secure cloud repository. In selected samples, additional staining such as Masson's trichrome was performed to assess collagen deposition and fibrotic remodeling.

ILD histopathology scoring system

A structured 12-parameter histopathology scoring system was applied to whole-slide images (WSIs) of lung sections to capture the spectrum of ADC-induced interstitial lung disease (ILD) pathology. Each parameter was graded semi-quantitatively on a 0 – 3 scale, where 0 = normal (<5% of lung parenchyma involved), 1 = mild (5 – 33%), 2 = moderate (33 – 66%), and 3 = marked (>66%). The system encompassed three domains of pathology. Acute inflammatory features included alveolar inflammation, defined as neutrophils and activated macrophages within alveolar spaces and septa, lymphocytic infiltration in the interstitium or peribronchial regions, mononuclear cell infiltration, characterized by foamy or pigment-laden macrophages and granulomas, defined as well-formed epithelioid histiocyte aggregates with or without giant cells, scored separately as 0 = none, 1 = rare, 2 = multiple small foci, or 3 = numerous/confluent. Vascular and interstitial alterations included perivascular or interstitial edema, pulmonary congestion (capillary and venous engorgement), hemorrhage (extravasated erythrocytes in alveolar or interstitial spaces), and microthrombi, defined as fibrin-rich occlusive thrombi in small vessels and scored as 0 = none, 1 = 1 – 2 thrombi per lobe, 2 = 3 – 5 per lobe, or 3 = >5 per lobe or confluent distribution. Chronic and remodeling features included peribronchial wall thickening due to smooth muscle and stromal expansion, intra-alveolar or interstitial fibrin deposition (confirmed by special stains where necessary), pulmonary fibrosis defined as collagenized interstitium with architectural distortion, and type II pneumocyte hyperplasia, scored by the proportion of alveolar surface lined by reactive cuboidal epithelium. Scoring was performed on WSIs at low power with high-power confirmation, surveying all lobes. Scores per animal reflected the aggregate of all lobes. If lobes were scored separately, values were averaged per animal. A composite ILD severity score (range 0–36) was calculated by summing the 12 parameters, and a mean injury score (range 0–3) was derived by dividing the composite score by 12. All slides were digitally coded and reviewed by a board-certified veterinary pathologist blinded to treatment assignment to minimize bias. For focal or binary lesions such as granulomas and microthrombi, explicit count-based categories were used when lesions were sparse, while percent area scoring was applied when lesions were extensive or confluent. To ensure consistency, airways >2 mm and large

vessels were excluded from parenchymal calculations, while terminal bronchioles were included. When edema and hemorrhage co-localized, each was scored independently if thresholds were met. For fibrosis, only regions with architectural distortion were prioritized, while perivascular stromal thickening alone was not scored as fibrotic.

Synthesis of MC-GGFG-Cy

To the solution of cyclohexyl amine (10 mg, 0.101 mmol, 1 eq) and MC-GGFG-CH_2-O-CH_2COOH (CAS: 1599440-25-1) (69.1 mg, 0.112 mmol, 1.1 eq) in anhydrous DMF at RT, NMM (0.014 mL, 0.126 mmol, 1.25 eq) was added, followed by DMTMM (55.8 mg, 0.126 mmol, 1.25 eq). The reaction was stirred at room temperature until the consumption of the starting material. After 10 min, diluted with (1:1) water: acetonitrile and purified via reverse phase C18 (50 g) using water: acetonitrile (0.05% FA). The product fractions were combined and lyophilized to get MC-GGFG-Cy (46 mg, 65% yield) as a white solid. (ESI) m/z: $[M + H]^+ = 698.41$. ^{1}H NMR (500 MHz, DMSO) δ 8.65 (t, J = 6.6 Hz, 1H), 8.35 (t, J = 5.9 Hz, 1H), 8.16 (d, J = 7.9 Hz, 1H), 8.08 (t, J = 5.7 Hz, 1H), 8.02 (t, J = 5.7 Hz, 1H), 7.54 (d, J = 8.2 Hz, 1H), 7.28 – 7.21 (m, 4H), 7.20 – 7.15 (m, 1H), 7.00 (s, 2H), 4.56 (d, J = 6.6 Hz, 2H), 4.52 – 4.44 (m, 1H), 3.81 (s, 2H), 3.74 (ddd, J = 9.5, 8.9, 4.7 Hz, 3H), 3.67 (t, J = 5.0 Hz, 2H), 3.59 (dd, J = 16.7, 5.5 Hz, 2H), 3.38 – 3.35 (m, 2H), 3.06 (dd, J = 13.8, 4.4 Hz, 1H), 2.80 (dd, J = 13.8, 9.8 Hz, 1H), 2.14 – 2.07 (m, 2H), 1.74 – 1.61 (m, 4H), 1.57 – 1.42 (m, 5H), 1.28 – 1.15 (m, 6H), 1.12 – 1.02 (m, 1H).

Calculation of drug to antibody ratio (DAR)

To determine the DAR of the conjugates by RP-LC/MS, 0.5 µg of ADC was injected onto a PLRP-S column (1000 Å, 8 µm, 2.1 × 50 mm) on a Waters Acquity UPLC running a 25 – 45% gradient (ACN :Water + 0.1% formic acid; 0.35 mL/min flow) connected to a Xevo G2-XS QTof mass spectrometer. Monomeric purity of the ADC's was determined by size exclusion chromatography (SEC); 20 µg of ADC was injected on a TSKgel3000SWXL column running an isocratic method of PBS pH 7.4 with 10% IPA at a flow of 0.8 mL/min. Purification of ADCs was performed either by preparative SEC followed by tangential flow filtration (TFF), or TFF alone. SEC purification was performed on an AKTA Avant using a Hiload™ 26/600 Superdex™ 200 pg column with isocratic 1× PBS as the mobile phase at 2.6 mL/minute. TFF was performed with a Sartorius 30,000 MWCO HY cassette. ADCs were buffer exchanged into 20 mM histidine, pH 5.5, with 6 – 10 diavolumes. Following purification, ADCs were concentrated with 30 KDa MWCO spin concentrators to the working concentration before being passed through a 0.2 µm filter and aliquoted for analysis and storage. Final analysis was performed as previously written, with the additional step of reducing 10 µg of ADC with dithiothreitol for DAR analysis by LC–MS. LC–MS spectra was deconvoluted and signals were used in the below formula (Eq. 1) for DAR determination.

$$DAR = 2\left(\frac{\Sigma(n * L_n)}{\Sigma(L_n)} + \frac{\Sigma(n * H_n)}{\Sigma(H_n)}\right) \quad (1)$$

LC–MS DAR Calculation- where n is the number of linker–payloads attached. *Ln and Hn* refer to the signal intensities of the light(L) and heavy(H) species with respect to the number of linker–payloads attached.

Statistical analysis

All statistical analyses were conducted using GraphPad Prism (v10.0 or later). Data are presented as mean ± standard deviation. Prior to hypothesis testing, data distributions were assessed for normality using the Shapiro-Wilk test. For group-wise comparison, a Kruskal–Wallis test followed by Dunn's post hoc multiple comparison test was applied. A p-value of <0.05 was considered statistically significant. In figures, significance levels are indicated as follows: (*) represents p values between 0.01 and 0.05, and (**) represents p-values between 0.001 and 0.01.

Data availability

All data supporting the findings of this study, including histopathology scoring sheets, incidence tables, and representative whole-slide images, are available upon reasonable request from the corresponding authors.

Received: 22 December 2025; Accepted: 28 April 2026;
Published online: 21 May 2026

References

1. Nguyen, T. D., Bordeau, B. M. & Balthasar, J. P. Mechanisms of ADC toxicity and strategies to increase ADC tolerability. *Cancers* **15**, 713 (2023).
2. Khongorzul, P., Ling, C. J., Khan, F. U., Ihsan, A. U. & Zhang, J. Antibody-drug conjugates: a comprehensive review. *Mol. Cancer Res.* **18**, 3–19 (2020).
3. Joubert, N., Beck, A., Dumontet, C. & Denevault-Sabourin, C. Antibody-drug conjugates: the last decade. *Pharmaceuticals (Basel)* **13**, 245 (2020).
4. Beck, A., Goetsch, L., Dumontet, C. & Corvaïa, N. Strategies and challenges for the next generation of antibody-drug conjugates. *Nat. Rev. Drug Discov.* **16**, 315–337 (2017).
5. Perez, J. et al. Trastuzumab Deruxtecan in HER2-positive metastatic breast cancer and beyond. *Expert Opin. Biol. Ther.* **21**, 811–824 (2021).
6. Powell, C. A. et al. Pooled analysis of drug-related interstitial lung disease and/or pneumonitis in nine Trastuzumab Deruxtecan monotherapy studies. *ESMO Open.* **7**, 100554 (2022).
7. Soares, L. R. et al. Incidence of interstitial lung disease and cardiotoxicity with Trastuzumab Deruxtecan in breast cancer patients: a systematic review and single-arm meta-analysis. *ESMO Open.* **8**, 101613 (2023).
8. Kawakami, H. et al. EN-DEAVOR Study Group. Real-world effectiveness and safety of Trastuzumab-Deruxtecan in Japanese patients with HER2-positive advanced gastric cancer (EN-DEAVOR study). *Gastric Cancer* **28**, 51–61 (2025). Erratum in: Gastric Cancer. 28(1):62 (2025).
9. Goldenberg, D. M., Cardillo, T. M., Govindan, S. V., Rossi, E. A. & Sharkey, R. M. Trop-2 is a novel target for solid cancer therapy with sacituzumab govitecan (IMMU-132), an antibody-drug conjugate (ADC). *Oncotarget* **6**, 22496–22512 (2015). Erratum in: Oncotarget. 11(10):942 (2020).
10. Bardia, A. et al. Sacituzumab Govitecan-hziy in refractory metastatic triple-negative breast cancer. *N. Engl. J. Med.* **380**, 741–751 (2019).
11. Wang, R. et al. Antibody-drug conjugates (ADCs): current and future biopharmaceuticals. *J. Hematol. Oncol.* **18**, 51 (2025).
12. Kumagai, K. et al. Interstitial pneumonitis related to Trastuzumab Deruxtecan, a human epidermal growth factor receptor 2-targeting Ab-drug conjugate, in monkeys. *Cancer Sci.* **111**, 4636–4645 (2020).
13. Sloot, W. N. et al. The nonclinical safety assessment of a novel anti-CEACAM5 Antibody exatecan conjugate predicts a low risk for interstitial lung disease (ILD) in patients—the putative mechanism behind ILD. *Int-. J. Toxicol.* **44**, 153–169 (2025).
14. Abuhelwa, Z., Alloghbi, A., Alqahtani, A. & Nagasaka, M. Trastuzumab deruxtecan-induced interstitial lung disease/pneumonitis in ERBB2-positive advanced solid malignancies: a systematic review. *Drugs* **82**, 979–987 (2022).
15. Peters, S., Parikh, K., Dimou, A. & Desai, A. 3P Correlation between antibody-drug conjugate (ADC) targetable antigen expression and occurrence of interstitial lung disease (ILD). *ESMO Open* **8**, 100969 (2023).
16. Cortés, J. et al. DESTINY-Breast03 Trial Investigators. Trastuzumab Deruxtecan versus Trastuzumab Emtansine for breast cancer. *N. Engl. J. Med.* **386**, 1143–1154 (2022).
17. Koganemaru, S. et al. Potential mechanisms of interstitial lung disease induced by antibody-drug conjugates based on quantitative analysis of drug distribution. *Mol. Cancer Ther.* **24**, 242–250 (2025).

18. Modi, S. et al. DESTINY-Breast01 investigators. trastuzumab deruxtecan in previously treated HER2-positive breast cancer. *N. Engl. J. Med.* **382**, 610–621 (2020).
19. Tamura, K. et al. Trastuzumab Deruxtecan (DS-8201a) in patients with advanced HER2-positive breast cancer previously treated with Trastuzumab emtansine: a dose-expansion, phase 1 study. *Lancet Oncol.* **20**, 816–826 (2019). Erratum in: Lancet Oncol. 20(6):e293 (2019).
20. Baba, T. et al. Clinical and imaging features of interstitial lung disease in cancer patients treated with Trastuzumab Deruxtecan. *Int. J. Clin. Oncol.* **28**, 1585–1596 (2023). Erratum in: Int J Clin Oncol. 29(1):78-79 (2024).
21. Udagawa, C. et al. Whole genome sequencing to identify predictive markers for the risk of drug-induced interstitial lung disease. *PLoS ONE* **14**, e0223371 (2019).
22. Ogura, T. et al. DLD/TO Assemblies of JRS. Summary of the Japanese Respiratory Society statement for the treatment of lung cancer with comorbid interstitial pneumonia. *Respir. Investig.* **57**, 512–533 (2019).
23. Kadam, A. H. & Schnitzer, J. E. Highly Calibrated Relationship Between Bleomycin Concentrations and Facets of the Active Phase Fibrosis in Classical Mouse Bleomycin Model. *Int. J. Mol. Sci.* **25**, 12300 (2024).
24. Hübner, R. H. et al. Standardized quantification of pulmonary fibrosis in histological samples. *Biotechniques* **44**, 507–517 (2008).
25. Silva, I. A. N. et al. A semi-quantitative scoring system for green histopathological evaluation of large animal models of acute lung injury. *Bio Protoc.* **12**, e4493 (2022).
26. Klopfleisch, R. Multiparametric and semiquantitative scoring systems for the evaluation of mouse model histopathology—a systematic review. *BMC Vet. Res.* **9**, 123 (2013).

Acknowledgements

In vivo studies were performed by Lab to Pharmacy (L2P Research, Now part of NJ Bio, Inc.), 25 Health Sciences Drive, Stony Brook, NY 11790, USA, under contract with NJ Bio Inc. The authors acknowledge the contributions of Rachel Fernandes and Bhushan Satam in figure preparation and paper formatting. All histology tissue embedding and digital slide scanning were performed under contract by Histowiz Inc., New York, USA, in accordance with standard laboratory procedures.

Author contributions

J.D. and N.J. conceived and designed the study. S.A., J.P., A.B., and S.M. developed the methodology. S.A. and J.P. performed the in vivo studies and histopathological investigations. Chemical synthesis and preparation of test articles were carried out by J.D., N.J., A.B., S.M., N.P., A.W., and R.V. Data curation and analysis were performed by S.A., Z.S., and N.P. S.A. wrote the original draft of the paper. J.D., N.J., and all authors contributed to reviewing and editing the paper. J.D. and N.J. supervised the study. All authors reviewed the paper and approved the submitted version. All authors agree to all paper contents, the author list and its order, and the author contribution statements.

Competing interests

N.J. and S.A. are shareholders of NJ Bio, Inc. All authors were employees of NJ Bio, Inc. while performing the study. Patent application pertaining to the ADCs NJB-T-PL30, NJB-T-PL119, NJB-T-PL90, and NJB-T-PL10 (Application # WO2025/222127 A2) is currently pending. N.J., S.M., N.P., R.V., Z.S., A.B., and A.W. are listed as inventors. NJ Bio, Inc. is the applicant for this patent.

Additional information

Supplementary information The online version contains supplementary material available at https://doi.org/10.1038/s41698-026-01465-3.

Correspondence and requests for materials should be addressed to Suresh Anaganti or Julien Dugal-Tessier.